A Severe Weather Quick Observing System Simulation Experiment (QuickOSSE) of Global Navigation Satellite System (GNSS) Radio Occultation (RO) Superconstellations

S. MARK LEIDNER, THOMAS NEHRKORN, JOHN HENDERSON, AND MARIKATE MOUNTAIN

Atmospheric and Environmental Research, Verisk Analytics, Lexington, Massachusetts

TOM YUNCK

GeoOptics, Inc., Pasadena, California

ROSS N. HOFFMAN

Atmospheric and Environmental Research, Verisk Analytics, Lexington, Massachusetts, and Cooperative Institute for Marine and Atmospheric Studies, University of Miami, and NOAA/Atlantic Oceanographic and Meteorological Laboratory, Miami, Florida

(Manuscript received 4 June 2016, in final form 13 September 2016)

ABSTRACT

Global Navigation Satellite System (GNSS) radio occultations (RO) over the last 10 years have proved to be a valuable and essentially unbiased data source for operational global numerical weather prediction. However, the existing sampling coverage is too sparse in both space and time to support forecasting of severe mesoscale weather. In this study, the case study or quick observing system simulation experiment (QuickOSSE) framework is used to quantify the impact of vastly increased numbers of GNSS RO profiles on mesoscale weather analysis and forecasting. The current study focuses on a severe convective weather event that produced both a tornado and flash flooding in Oklahoma on 31 May 2013. The WRF Model is used to compute a realistic and faithful depiction of reality. This 2-km ''nature run'' (NR) serves as the ''truth'' in this study. The NR is sampled by two proposed constellations of GNSS RO receivers that would produce 250 thousand and 2.5 million profiles per day globally. These data are then assimilated using WRF and a 24-member, 18-km-resolution, physics-based ensemble Kalman filter. The data assimilation is cycled hourly and makes use of a nonlocal, excess phase observation operator for RO data. The assimilation of greatly increased numbers of RO profiles produces improved analyses, particularly of the lower-tropospheric moisture fields. The forecast results suggest positive impacts on convective initiation. Additional experiments should be conducted for different weather scenarios and with improved OSSE systems.

1. Introduction

The benefits of assimilating radio occultation (RO) observations for weather forecasting that were predicted 20 years ago (e.g., Ware et al. 1996), have been definitively demonstrated in recent years in several areas. For example, research investigations using observations from the COSMIC (all acronyms are defined in the appendix) constellation of Global Navigation Satellite System (GNSS) RO satellites have examined potential improvements in forecasting western Pacific typhoons (e.g., Chen et al. 2015) and atmospheric rivers (e.g., Ma et al. 2011) in observing system experiments (OSEs). Further, the positive effects of GNSS RO on global operational weather forecasting have been demonstrated extensively at NCEP (Cucurull et al. 2007; Cucurull and Derber 2008) and ECMWF (Healy 2008). It is noteworthy that, compared to typical passive space-based observing systems, RO satellites provide great absolute accuracy with essentially no bias and high vertical resolution. However, until the current study, the impacts of RO observations on severe convective weather forecasts had not been investigated. The work described here breaks new ground in two significant ways compared with previous RO data impact studies. First, we examine small spatial scales and

Corresponding author e-mail: Ross N. Hoffman, ross.n.hoffman@aer.com

DOI: 10.1175/MWR-D-16-0212.1

© 2017 American Meteorological Society

phenomena relevant to severe weather. Second, we consider very large RO superconstellations (ROSCs, pronounced ''Ross Seas''). Of course, such large constellations do not yet exist. Consequently, this study is performed in simulation using an observing system simulation experiment (OSSE) approach. That is, the observations are simulated from a known ''true'' atmospheric state defined by a realistic, high-resolution model run. Then the impact of using observations from future hypothetical RO observing systems is tested in an environment where the ''truth'' is known.

A current limitation on severe weather forecasting is our ability to initialize the forecast model. Because of the small spatial and temporal scales of deep convection, the initial conditions of a regional weather forecast are usually underdetermined; that is, there are not enough observations, either in terms of density or frequency, to define the initial state of the atmosphere. Doppler weather radar has provided the most frequent sampling of the 3D troposphere in time and space. However, weather radars 1) have viewing geometries that miss significant parts of the local atmosphere; 2) require the presence of atmospheric scatterers (usually hydrometeors); 3) have significant quality issues (range folding, anomalous propagation, ducting, etc.); and, most importantly, 4) primarily measure reflectivity and the motion (i.e., the wind) field but do not help to directly define the thermodynamic state (i.e., the temperature and humidity) of the atmosphere. In addition to ground-based radars, future microwave and hyperspectral infrared sensors in geostationary orbit (e.g., Bingham et al. 2013; Lambrigtsen 2015) or on constellations of many, perhaps 15–20, small satellites (e.g., Atlas and Pagano 2014; Maschhoff 2015), may, if design goals are met, provide substantial amounts of high-quality high-vertical-resolution thermodynamic profiles and large numbers of atmospheric motion vectors down to cloud top to improve the specification of the initial conditions for storm-scale forecasts.

In contrast, RO observations inherently have high accuracy and high vertical resolution. Proposed superconstellations of low-cost, low Earth orbit (LEO) GNSS RO satellites would therefore afford the opportunity to sample the atmosphere accurately and with vertical detail at much higher frequency and horizontal resolution than is possible with the current global observing network of ground-based sensors and satellites. An RO satellite ''listens'' for signals from GNSS satellites and observes the time it takes for the signal to traverse the limb of the atmosphere. The six orbiting COSMIC satellites currently gather about 1400 vertical occultation profiles every day globally. The COSMIC follow-on constellation, COSMIC-2, if fully deployed (12 satellites) will produce 8000–10 000 global profiles per day. (The six COSMIC-2A satellites in near-equatorial orbits are expected to launch in September 2017. The six COSMIC-2B satellites in high inclination orbits are scheduled to launch in 2019, but are not funded as of this writing.) The significant increase of observations made by COSMIC-2 should produce measurable improvements in global weather forecast models, but perhaps only very modest improvements in small-scale regional weather models, where the sampling requirements in space and time are much more stringent (on the order of 2 vs 20 min and 2 vs 20 km).

Here, we consider the potential impact of very much larger constellations on weather forecasting—ROSCs comprising hundreds to a thousand receiving units in orbit instead of 6, 12, or 18. The maximum constellation considered in this study (ROSC-2.5M) would yield roughly 2.5 million vertical occultation profiles, every day, globally. For comparison, the COSMIC mission gathers about one vertical radio occultation profile over the state of Oklahoma every other day, while ROSC-2.5M would include 35–50 vertical profiles over the state of Oklahoma every hour. With this observation technology, improved estimates of the 3D mass field are possible globally, in all weather conditions, at horizontal resolution of 10–20 km with a refresh rate on the order of 100 min. This is an order of magnitude better both spatially and temporally compared to the current observing system.

In this case study, we explore whether the assimilation of dense radio occultation observations can improve the depiction of preconvective environments, which might then translate into improved convective initiation and, potentially, improved warnings of severe weather outbreaks [see Stensrud et al. (2009) for a discussion of ''warn-on-forecast'']. The accurate depiction of humidity in the preconvective environment, specifically in the lower troposphere and boundary layer, is a critical factor in forecasting severe weather. GNSS RO is particularly relevant to improving the humidity initial conditions for severe weather because it is unaffected by clouds and extremely sensitive to water vapor. This sensitivity is a reflection of the fact that as Melbourne et al. (1994, p. xii) note ''[t]he refractivity of a mole of water vapor for microwaves is about 17 times that of dry air.''

GNSS RO does not directly observe humidity. Rather, GNSS RO observes refractivity or bending angle or phase delay with high precision and no ambiguity, virtually down to the surface (Kursinski et al. 1997). Refractivity depends on temperature and humidity. In drier parts of the atmosphere temperature can be retrieved alone. However, due to the aforementioned sensitivity, in moist parts of the atmosphere (below about 7–8 km in the tropics and 3–6 km in the midlatitudes), RO observations are primarily affected by humidity. In earlier studies (e.g., Kursinski et al. 1997;

Kursinski and Hajj 2001), accurate humidity profiles in the lower troposphere were retrieved by making use of modeled temperature profiles. Zou et al. (1995) showed a strong positive impact of RO observations on the moisture field in an OSSE for a winter storm using a 60-km regional four-dimensional variational (4D-Var) data assimilation (DA) system. Cucurull and Derber (2008) reported improvements due to the assimilation of COSMIC observations on the depiction of moisture, especially on the bias in the Southern Hemisphere, in preoperational tests of the May 2007 NCEP global DA system. Recently, Li et al. (2015) demonstrated detection of strong humidity gradients accompanying severe weather phenomena using ground-based multiconstellation GNSS observations. In the present study, because of the use of an ensemble of short-term forecasts to estimate the error covariance of all model variables, the DA system extracts both temperature and humidity information from the RO observations in a near-optimal fashion.

The plan of this paper is the following: the WRF mesoscale modeling system, including the ensemble Kalman filter (EnKF) data assimilation package, is described in section 2. The simulation of the ROSC observations is described in section 3. The case study selected and the experimental setup is described in section 4, and results of these experiments are given in section 5. Section 6 provides a summary and conclusions, including a discussion of the limitations of this study. We note here that the chief limitations of this study are 1) there is only one case, 2) this is a fraternal twin experiment, and 3) the OSSE system has not been fully validated.

2. Data assimilation system

The DA system used combined WRF and DART (''lanai'' release; Data Assimilation Research Section 2016), which includes the GNSS RO nonlocal, excess phase forward operator described in section 3. WRF-DART implements an EnKF to estimate localized, flow-dependent background error covariances. In our experiments a 24-member, multiphysics ensemble of WRF forecasts is used and DART updates all WRF prognostic variables, including hydrometeors. This configuration is similar to that of several other real data studies (e.g., Yussouf et al. 2013b; Jirak et al. 2014; Jones et al. 2015; Schwartz et al. 2015a) and OSSEs (e.g., Jones et al. 2013; Kerr et al. 2015). A similar setup of WRF-DART is being developed as a prototype warn-on-forecast system and has been tested on six cases including the El Reno, Oklahoma, case studied here (Wheatley et al. 2015; Jones et al. 2016). At selected analysis times longer forecasts are made using a single set of physics parameterizations. The WRF configurations detailed below are summarized in Table 1.

a. Forecast model

The Weather Research and Forecasting (WRF) Model (Skamarock and Klemp 2008; Skamarock et al. 2008) modeling system is a regional, relocatable, weather forecasting system. WRF version 3.5.1 is used in this study. As a ''community model,'' WRF has many options for parameterizations of the physical processes that are not explicitly resolved. The choice of parameterizations depends strongly on the horizontal scale, region of the world, and the particular phenomena of interest. As is evident from many studies in the literature, the optimal physical parameterizations would be very different for weather near the equator, in the Arctic, over all of North America, or along the Florida coastline in summer, where the sea-breeze front may be the primary initiator of convection. For mesoscale ensemble DA, using appropriate, but different physics parameterizations in each ensemble forecast has been shown to be helpful in several studies (Stensrud et al. 2000; Fujita et al. 2007; Yussouf et al. 2013a). For our experiments we use the physics options for WRF-DART ensemble members that were used in the NSSL Mesoscale Ensemble (NME; Jirak et al. 2014) system as implemented for the 2013 Spring Experiment, with one exception. Compared with the NME 32-member ensemble, we reduced the ensemble size to 24 (and reduced the computational burden) by eliminating the least up-to-date (longwave and shortwave) radiative transfer parameterizations from those used in the NME ensemble. Thus, as shown in Table 1, the forecast ensemble members in this study use all combinations of two radiative parameterizations [RRTMG (Iacono et al. 2008) and Goddard (Chou and Suarez 1999; Chou et al. 2001)], four PBL parameterizations [YSU (Hong et al. 2006), MYJ (Janjić 1994, 2002), MYNN (Nakanishi and Niino 2006, 2009), and ACM2 (Pleim 2007a,b)], and three cumulus parameterizations [Kain–Fritsch (Kain and Fritsch 1993; Kain 2004), Grell–Freitas (Grell and Freitas 2014), and Tiedtke (Tiedtke 1989; Zhang et al. 2011)]. The Noah land surface model (Ek et al. 2003; Tewari et al. 2004) is used throughout except for members that use the ACM2 PBL configuration, which must be paired with the Pleim–Xiu land surface model (Xiu and Pleim 2001; Pleim and Xiu 2003; Gilliam and Pleim 2010). The longer nonensemble forecasts all used the single combination of RRTMG radiation, MYNN PBL, and (in the 18-km domain only) Grell–Freitas cumulus parameterization. The NR also uses the RRTMG radiation, but uses the ACM2 PBL, and no cumulus parameterization. In all cases the Thompson microphysics parameterization (Thompson et al. 2004, 2008) is used. In all WRF runs reported here, 51

TABLE 1. WRF configurations. The table entries are grouped into three categories: physics submodels; resolution and other WRF specifications; and input data. Square brackets and rightward arrows indicate one-way parent–child grid nesting (i.e., parent[→ child]).

WRF submodels, settings, and data	Forecast ensemble members	Longer nonensemble forecasts	Nature run
Radiation	RRTMG Goddard	RRTMG	RRTMG
PBL	YSU MYJ MYNN ACM2	MYNN	ACM2
Cumulus	Kain–Fritsch Grell–Freitas Tiedtke	Grell–Freitas[a]	None
Microphysics	Thompson	Thompson	Thompson
Land surface	Noah[b]	Noah	Pleim–Xu
Vertical levels	51	51	51
Grid nesting	None	Domains: 1[→ 2[→ 3]][c]	Domains: 1[→ 2][c]
Horizontal resolution	18 km	18[→ 6[→ 2]] km	6[→ 2] km
Time step	45 s	45[→ 15[→ 5]] s	18[→ 6] s
Grid nudging	None	None	None
Initial conditions	Ensemble analyses[d]	Ensemble analysis[e]	NAM 12-km analysis
Boundary conditions	NAM 12-km analysis	NAM 12-km analysis	NAM 12-km analysis
Surface parameters	NAM 12-km analysis	NAM 12-km analysis	NAM 12-km analysis

[a] In the 18-km domain only.
[b] Except that PLEIM–Xu is used with ACM2 PBL.
[c] Nested grids turn on at the initial time.
[d] The NAM 12-km analysis is used for the first cycle.
[e] The member closest to the ensemble mean is used.

vertical levels are used, surface and lateral conditions are provided by NAM 12-km analysis, and nested runs all use one-way nesting with no grid nudging and with the inner nests interpolated from the outer nest at the initial time. For the NR, time steps of 18 s are used with the 6-km grid and 6 s with the 2-km grid. Otherwise, time steps of 45, 15, and 5 s are used with the 18-, 6-, and 2-km grids, respectively.

The NR and forecast models used in this study are fraternal twins—they share the same dynamical core, but some physical parameterizations are different. Referring to Table 1, the models used in the data assimilation all parameterize convection and have a horizontal grid resolution of 18 km, while the NR model has explicit convection and much smaller grid spacing. Compared to the model used for the longer nonensemble forecasts, the NR has a different PBL parameterization and a different land surface model.

b. Data assimilation

DA is a cyclic process that combines prior information embodied in a forecast (or ensemble of forecasts) and recently collected observations to produce an analysis. The optimal combination (i.e., the best analysis) depends on the estimates of the errors of the forecast and of the observations. There are many approaches to DA (Kalnay 2002) and here we use the EnKF as implemented in the WRF-DART DA system (Anderson et al. 2009). The ensemble approach, used by itself (e.g., Snook et al. 2015) or in a hybrid system (e.g., Pan et al. 2014), allows for background error covariance to be flow dependent, a substantial advance over static climatological estimates of background error covariance, especially for severe weather DA where small, intense, mobile features result in complex and evolving error covariance patterns.

For efficiency relatively small ensembles are generally used in EnKF. However, this results in spurious long-range correlations in the ensemble estimate of the forecast error covariance. One practical solution, the localization of the ensemble covariances (Greybush et al. 2011), is used in WRF-DART. In this work, the horizontal localization radius was subjectively tuned to 300 km using single observation analysis tests to match the approximate pathlength of the midtropospheric portion of an RO ray. A typical RO profile contains 2000–3000 vertical levels. These are thinned to 32 levels below 15 km above ground level (AGL) before being assimilated. The thinning strategy selects vertical levels so that first Fresnel zone diameters (corresponding roughly to the vertical and horizontal cross section of the measurement), computed from a *U.S. Standard Atmosphere, 1976* (COESA 1976), do not overlap, reducing or eliminating a significant source of observation error correlation from oversampling within a profile. Since the simulated data are free of gross errors, no quality control (QC) procedures are applied.

3. Simulation of radio occultations profiles

The shape and volume of the atmosphere measured by each ray during a single set of occultation measurements (~2000 in the vertical) is peculiar to limb soundings. At successively deeper layers in the atmosphere, the Fresnel diameter decreases from about 1.5 km at 60 km to ~100 m at 1 km (Hajj et al. 2002), but the signal-to-noise ratio also decreases as the perigee or tangent point (TP) of the ray moves closer to Earth's surface, from 300–400 at 60 km to 20–30 at 1 km. The horizontal path in the occultation plane has an effective measurement length of about 100 km in the upper troposphere to 400–500 km in the lower troposphere [cf. Fig. 7 from Poli (2004)]. Each ray therefore measures a long, narrow volume (about 1 km^2 in the cross section) that is bent along the ray path, with the maximum bending (refraction) occurring at the TP. With a dense sampling of the lower- and midtroposphere by GNSS RO, horizontal gradients in water vapor and temperature should be clearly positioned through the assimilation of RO measurements from a variety of azimuths, both parallel to and crossing the corresponding refractivity gradients.

Recent advances in data assimilation methods for GNSS RO data have produced so-called "nonlocal" forward models (or observation operators) that account for horizontal gradients in the occultation plane in the calculation of the model-equivalent quantity (e.g., Sokolovskiy et al. 2005). These are distinguished from "local" forward operators that assimilate refractivity or temperature at the TP only. Two recent studies have shown the benefits of using a nonlocal excess phase observation operator (Kunii et al. 2012; Ma et al. 2011). Excess phase is the difference between the pathlengths along the refracted ray and what would be observed in a vacuum. For reference, excess phase varies from as much as 2.5 km at the surface in the moist tropics to about 10 m in the lower stratosphere. The 2D observation operator of Sokolovskiy et al. (2005) is used both to simulate and assimilate observations. This observation operator integrates along straight ray paths through the WRF Model atmosphere passing through TP. For realism, random unbiased Gaussian errors are added to the "perfect" observations simulated from the NR. The standard deviation of these errors is specified as a fraction of the observed excess phase. This fraction ranges from 0.013 (1.3%) at the surface to 0.002 (0.2%) at 17 km [Liu et al. (2008), their Fig. 2 shows this between 2 and 10 km]. The nonlocal excess phase observation operator of Sokolovskiy et al. (2005) was added to the WRF-DART assimilation framework in 2008 (Chen et al. 2009).

Rather than simulate the orbits of the ROSC and the GNSS, we first collected the entire COSMIC sample of 36 478 occultation profiles observed during the period 20 May 2006–27 February 2014 in our regional modeling area (cf. section 4b). Figure 1 plots GNSS RO data coverage over the NR domain for three selections of observations. Each of the line segments in Fig. 1 colored from pink to yellow locates a single RO profile and indicates the altitude of the TP at the map position of the TP. The patterns seen in Fig. 1 arise because the TP drifts with the motion of the pair of satellites and as the transmitter rises (sets) in the sky as observed by the receiver, the TP altitude rises (sets). Note that the RO rays connecting the pair of satellites that make up the RO profile are generally at an oblique angle to the colored lines drawn in this figure. As evidenced by Fig. 1a, there are substantial regularities in the observing geometry in the COSMIC dataset. Such regularity would not occur in a ROSC. Consequently we randomize the occultation plane azimuths of the RO profiles as seen in the example of Fig. 1b. Then all these data are relabeled to times during the OSSE DA cycles (Fig. 1c) and thinned if necessary.

4. Design of experiments

The quick OSSE (QuickOSSE; Atlas et al. 2015) approach that is used in this study has several steps, which are described here. In contrast to a full OSSE, in which the NR is long enough to diverge completely from reality, a QuickOSSE NR is a short-term forecast of a real event of interest. In outline, for a QuickOSSE, a relevant forecast case is chosen, a high-resolution, high-accuracy forecast is produced to serve as the NR, data are simulated for the various observing systems, and then several DA and forecast experiments are run. The first, called the Control experiment, assimilates a baseline set of observations. Further experiments that add varying amounts of a new observation type to the control set of observations provide a way to gauge the impact as more and more of the new observation types are assimilated.

a. Case selection

For a high-impact severe weather case, we chose the El Reno event that produced a severe (EF3) tornado and flash flooding in the Oklahoma City, Oklahoma, metro area, late in the afternoon and early evening of 31 May 2013, from approximately 2100 UTC 31 May to 0300 UTC 1 June 2013. The El Reno tornado was the widest ever recorded

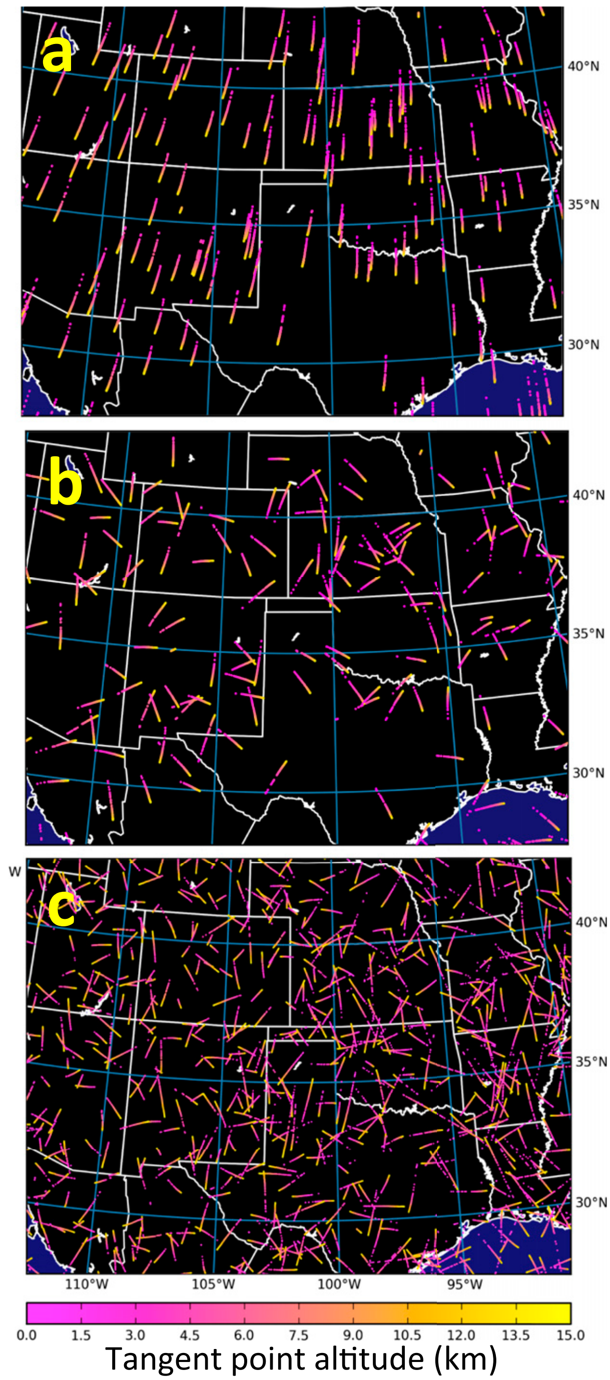

FIG. 1. GNSS RO data coverage over the NR domain for (a) all 178 rising occultations for GNSS satellite G22 during the 7.8-yr period 20 May 2006–27 Feb 2014. (b) As in (a), but with randomly rotated azimuths and with time compressed and reassigned to the interval 1130–1830 UTC 31 May 2013. (c) As in (b), but for the 766 occultation for all GNSS satellites during a 1-h period (1130–1230 UTC 31 May 2013).

(2.6 miles) and is very well documented (e.g., Wurman et al. 2014). This case was also sampled by the Mesoscale Predictability Experiment (MPEX; Weisman et al. 2015).

The prestorm environment was characterized by a southwest–northeast dryline that divided the state of Oklahoma with very dry air to the northwest and very moist, high latent energy air to the southeast. To paraphrase Schwartz et al. (2015b), the synoptic situation includes a broad 500-hPa trough, a deep occluded low over the northern plains, a mid- to upper-tropospheric front extending east and west through Kansas, a surface low pressure center in South Dakota, and a trailing cold front through the southern plains with an intersecting dryline. The air mass ahead of the cold front and dryline was very unstable and had strong vertical wind shear. The southern end of the line of convection that developed in Oklahoma remained stationary near El Reno, where a tornado developed around 2300 UTC. See Schwartz et al. (2015b, their Figs. 5–7) for a description of the overall event, Bluestein et al. (2015, their Figs. 1–3, 7) for a detailed description of the synoptic and mesoscale conditions, and Wurman et al. (2014) and Bluestein et al. (2015) for a detailed description of the tornado.

b. Nature run

The NR must be as realistic as possible since it is taken to be the truth in the QuickOSSE framework. Since our focus is on the development of precursors to severe convection, the depiction of a realistic dryline is critical. A 6-km convection-permitting NR from 0600 UTC 31 May to 1200 UTC 1 June 2013 was generated over the domain outlined in black in Fig. 2a, which covers a large part of the continental United States, with an inner 2-km nest (shown in red in Fig. 2a) that covers most of the state of Oklahoma, the primary area of interest for this study. Initial conditions for the NR are provided by NAM 12-km analysis.

Convection is slower to develop and evolve by an hour or two in the NR compared to reality, but the phenomenology and evolution of the convection and associated updraft helicity are strikingly similar to observed. These findings are from the hourly time series of NR and observed composite reflectivity, examples of which are included in Fig. 2. Note the agreement of the NR (Figs. 2b,c) to reality (Fig. 2d) is somewhat better when shifted backward in time by 2 hours.

c. Simulation of observations

In an OSSE, simulated observations must be generated with realistic coverage from the NR with added observation errors of the proper size. Conventional observations of altimeter setting, temperature, dewpoint, and horizontal wind components are simulated by evaluating the 6-km NR outer domain at the times and locations of

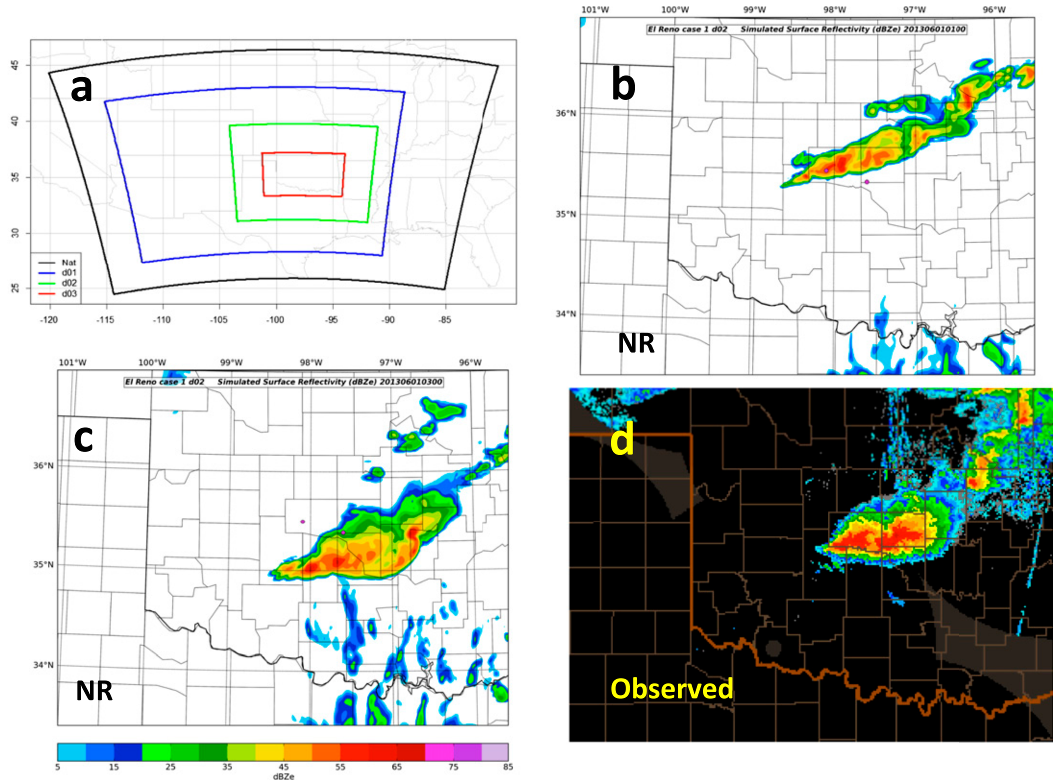

FIG. 2. The (a) NR and forecast model and DA domains used in the QuickOSSE, and the radar reflectivity (dBZ) on 1 Jun 2013 simulated in the NR at (b) 0100 and (c) 0300 UTC and (d) observed in reality at 0100 UTC. In (a) the 6- and 2-km NR domains are black and red, respectively; the 18-km DA system and ensemble forecast domain is blue; and the nested 18-, 6-, and 2-km forecast model domains are blue, green, and red, respectively.

the observations made in reality. Then, all available past GNSS RO observations are randomized and converted into ROSC ephemerides as described in section 3, from which synthetic excess phase RO observations are calculated from the NR using the forward operator in WRF-DART. Unbiased, uncorrelated observational errors are simulated with magnitudes consistent with the DART-assigned error standard deviation for each observation type. No radar observations were simulated because there are virtually no atmospheric scatterers present during the assimilation period, which ends before severe weather develops.

The three OSSE experiments conducted and the observations used in each are as follows:

- Control, which uses conventional observations, rawinsondes, land and marine surface observations, aircraft reports, and satellite-derived atmospheric motion vectors (AMVs);
- ROSC-250K, which uses all of the Control observations plus data from a ROSC yielding 250 000 global profiles per day; and
- ROSC-2.5M, which uses all of the Control observations plus data from a ROSC yielding 2.5 million global profiles per day.

ROSC-250K and ROSC-2.5M correspond to ROSCs of about 120 and 1200 RO listening satellites, respectively.

d. Experiment procedures

During the DA, WRF-DART is cycled to assimilate the synthetic observations using an ensemble of single-domain (not nested) forecasts at moderate 18-km resolution in a 118 $\times$ 90 gridpoint domain (blue outline in Fig. 2a) that is slightly smaller geographically than the 6-km nature run domain. This resolution was chosen because it is sufficiently fine to represent the environment for convective outbreaks but coarse enough to keep computational costs manageable. In each experiment the DA cycling is hourly beginning at 1200 UTC and ending at 1800 UTC 31 May. To begin the data assimilation cycling, all 24 members start from the same NAM analysis as the NR at 0600 UTC 31 May 2013. This initial collapsed ensemble diverges substantially due to the different physics parameterizations by the start of the DA cycling at 1200 UTC 31 May 2013.

For the forecasts, we added one-way nested inner nests with resolutions of 6 km (with 183 $\times$ 156 grid

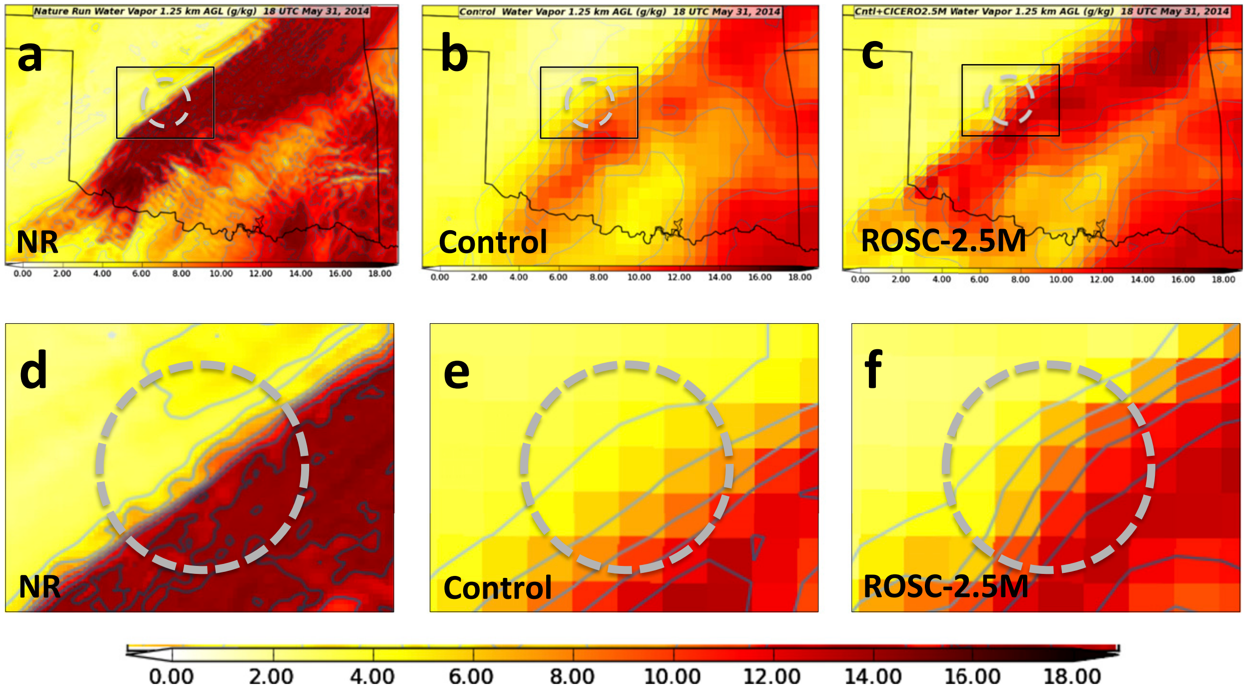

FIG. 3. Atmospheric water vapor (g kg^{-1}, color fill) at 1.25 km (approximately 4000 ft) AGL at 1800 UTC 31 May 2013 for (a) the NR, (b) the Control experiment analysis, and (c) the ROSC-2.5M experiment analysis. (d)–(f) Enlargement of the areas in (a)–(c) that are marked by the black rectangles. The gray dashed circle highlights the position of the dryline in the NR and is repeated at that position in the other panels. Note that the analyses in the DA experiments use a coarser 18-km grid than the 2-km nature run grid.

points, green outline in Fig. 2a) and 2 km (with 318 × 210 grid points, red outline in Fig. 2a). The 2-km NR and forecast grids are identical. This allows analysis and forecast verification without horizontal interpolation. To examine the impact of the observations on forecasts of the development of the preconvective environment and subsequent convection, forecasts are initialized after data assimilation and before convection have begun at 1400, 1600, and 1800 UTC 31 May. These forecasts end at 1200 UTC 1 June 2013, well after the first wave of convection has ended. Since the ensemble mean is the best estimate of the atmospheric state, but may be dynamically unbalanced, the initial state for each forecast is taken from the ensemble member closest to the ensemble mean determined with the rms normalized (actually, fractional) difference distance metric in the space defined by the WRF state vector. Many of these and other details of our experiments mirror the standard NSSL Spring Experiment practice.

5. Experiment results

The analyses and forecasts created for the different experiments are validated against the corresponding NR values.

a. Analysis impacts

Figure 3 shows snapshots from the NR, Control, and ROSC-2.5M experiments of lower-tropospheric water vapor—a key ingredient for severe weather. All are valid at 1700 UTC 31 May 2013 (i.e., 4–5 h before severe weather impacted Oklahoma City), and at 1.25 km above ground level. Figure 3a shows water vapor from the NR. The intense dryline seen in this realization of atmosphere moisture is the yardstick against which our assimilation experiments are compared for realism. Figure 3b and 3c compare the effects of using conventional weather observations versus conventional weather observations plus ROSC-2.5M observations. The ROSC-2.5M experiment that includes the RO observations produces a water vapor analysis (Fig. 3f) that is very much closer to the NR snapshot (Fig. 3d) in terms of the position and strength of the dryline than the Control experiment that uses only conventional weather observations (Fig. 3e).

In addition to improved specification of the atmospheric moisture field, assimilation of ROSC observations improves the analysis uncertainty. Figure 4 shows the water vapor mixing ratio analysis mean and uncertainty at ~ 140 m AGL valid at the start, middle, and end of the assimilation period for the Control and ROSC-2.5M experiments. In the ROSC-2.5M experiment the

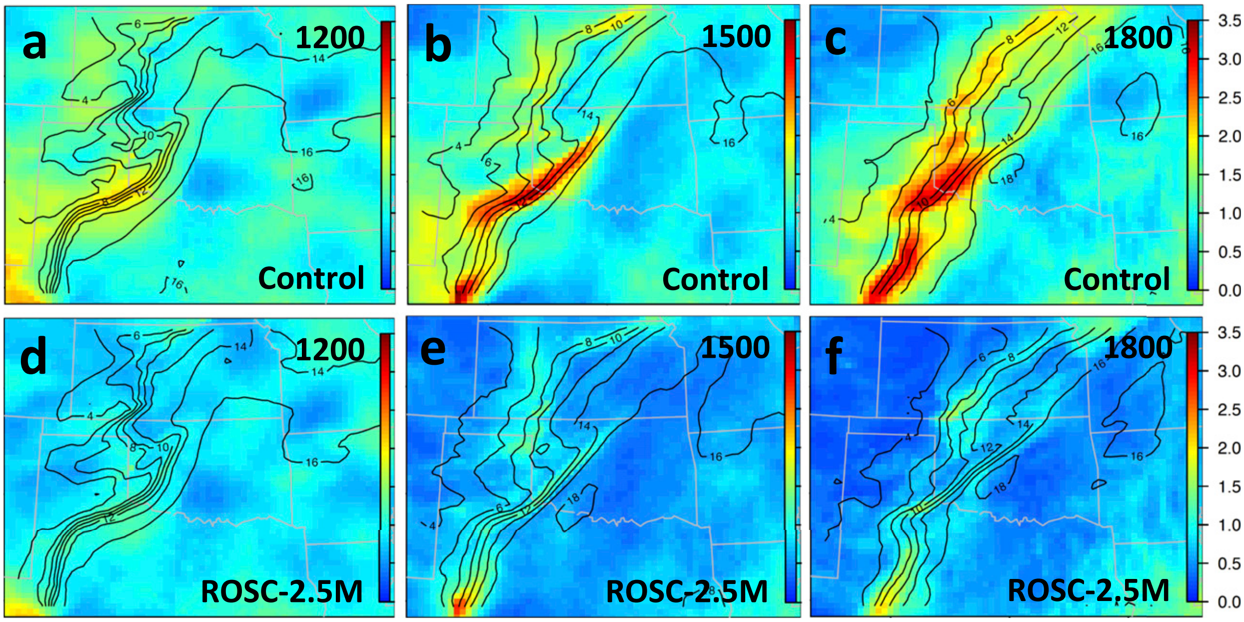

FIG. 4. The water vapor mixing ratio analysis uncertainty (g kg^{-1}, color fill) and analysis mean (g kg^{-1}, black contours) at ~ 140 m AGL valid at (a),(d) 1200; (b),(e) 1500; and (c),(f) 1800 UTC 31 May (i.e., at the end of the first, fourth, and seventh 1-h WRF-DART analysis cycles) for (a)–(c) the Control experiment and (d)–(f) the ROSC-2.5M experiment. The ensemble standard deviation is plotted in the colors shown by the color scale embedded on the right side of each panel, which runs from zero (blue) to 3.5 g kg^{-1} (red), with numeric values indicated on the right of (c) and (f).

uncertainty is much less immediately after the first assimilation cycle (cf. Figs. 4d and 4a). Then the uncertainty continues to decrease over the course of the experiment (from left to right in Fig. 4). However, in the Control experiment, without the benefit of the additional observations, the uncertainty increases in the strong gradient areas (cf. Figs. 4b,c and 4a). By the end of the assimilation, the dryline is much stronger (i.e., there is a sharper gradient represented by closer contours) and less uncertain (less yellow and red) in the ROSC-2.5M experiment (Fig. 4f) compared to the Control experiment (Fig. 4c).

The impact of ROSC observations on the analysis of lower-tropospheric temperature is similar to the impact on the moisture field, but the effects are more localized. After several hourly DA cycles, mesoscale features in the ROSC-2.5M analyses in the vicinity of the front are more clearly defined and represented compared to the Control experiment (not shown). As with analysis of the moisture field, uncertainty in the ROSC-2.5M temperature analyses is greatly reduced compared to the Control experiment.

Assimilating the ROSC observations also improved the fit to the conventional data. Figure 5 shows vertical profiles of the RMS difference of dewpoint between the simulated radiosonde observations and background (or guess) and the analysis for the Control and ROSC-2.5M experiments. Note that the impact on the analysis is more substantial than on the background. The RO data consistently improves the analysis of moisture, but during the 1-h forecast this improvement is degraded, possibly because there is little or no improvement in the wind analysis, which then has a negative impact as it advects the moisture analysis.

b. *Forecast impacts*

We verify the forecasts against the NR using maximum updraft helicity (UH), convective available potential energy (CAPE), and 2 m temperature. UH is computed as the maximum value (over the hour ending at the valid time) of $\mathscr{H}(t)$, where $\mathscr{H}(t)$ (in m^2 s^{-2}) is equal to vertical velocity times vertical vorticity integrated between two levels taken as 850 and 500 hPa in the results presented here. As in other studies (e.g., Clark et al. 2013), UH is taken to be a diagnostic for subgrid-scale severe weather and indicates the presence of rotating updrafts and, when persistent and sufficiently intense, long-track tornadoes. Also, by examining the effects for two constellation sizes—250 000 and 2 500 000 global profiles per day—we examine how the impact of the ROSC varies with observing density.

Highlights of the forecast impacts are the following. First, convective initiation and early convection morphology are improved by assimilating dense RO data. Second, most domain-averaged metrics remain significantly improved hours into the forecast. Figure 6

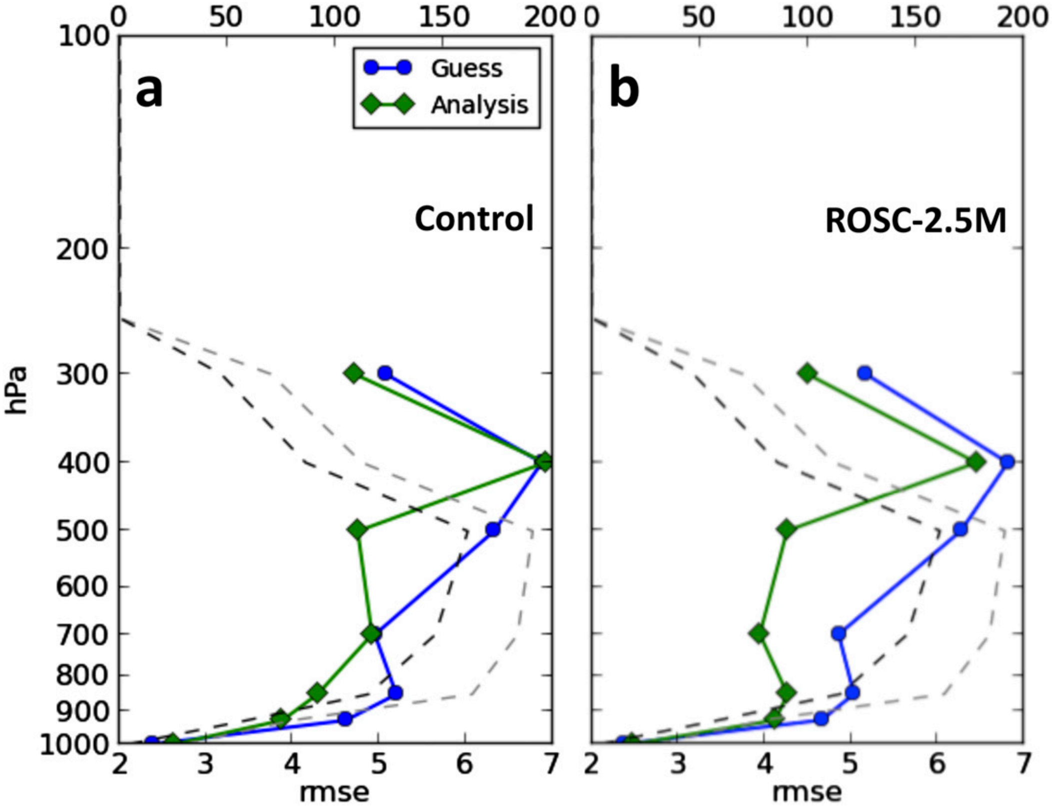

FIG. 5. Vertical profiles of RMS differences of radiosonde dewpoint (K) to the background ($O - B$, blue circles) and to the analysis ($O - A$, green diamonds) for (a) the Control experiment and (b) the ROSC-2.5M experiment. Dashed lines give the number of observations (top axis) available (gray) and passing QC and used (black) vs pressure level. Statistics (RMS differences and counts) are calculated over the 7 DA cycles (12–18 UTC 31 May 2013).

shows a number of RMS error statistics over the forecast model innermost domain calculated with the WRF Model Evaluation Toolkit (MET) Grid-Stat tool and using the NR as verification. The evolution of the RMS error values has a correspondence to the evolution of the NR convection. The line of convection seen in the NR-simulated radar reflectivity begins at 2100 UTC 31 May and becomes mature at 0100 UTC 1 June (Fig. 2b). Errors in CAPE and 2-m temperature are large during this period as convection develops. By 0600 UTC 1 June, the NR area of convection has substantially dissipated and largely moved out of the 2-km verification domain toward the southeast. Another line of convection begins to develop in the domain at 0700 UTC 1 June and reaches maturity at 1200 UTC 1 June. Errors in CAPE and 2-m temperature are again large during this period as convection develops. The trace of UH RMS error corresponds approximately to the strength of the convective activity seen in the radar reflectivity for the first convective event in the NR. There is no corresponding increase during the development of the second convective event presumably because strong UH is not present in this event. The lower CAPE errors for the free-running ''Nodata'' forecast (initiated at 0600 UTC) compared to the first few hours of the 1400 UTC (and less so for the 1600 UTC) Control and ROSC-2.5K forecasts reflect the benefit of the long spinup time in the Nodata forecast for CAPE. This relative advantage disappears with higher data volumes (ROSC-2.5M) and additional assimilation cycles (1600 and 1800 UTC). There are also smaller errors for the forecast Nodata 2-m temperature past 0200 UTC 1 June, but this is late in the forecast when the influence of the initial conditions is reduced and may be a sampling artifact that would not be present with a larger number of forecast cases.

It should be noted the forecast results are generally mixed and should be viewed as preliminary, in large part due to the chaotic nature of evolving convection. First, large samples are required to establish statistical significance, and a single case study can only hint at forecast impacts. Second, forecasts of convective events lack skill both because of model errors and initial errors. The ROSC OSSEs only improve initial errors, and the forecast impact

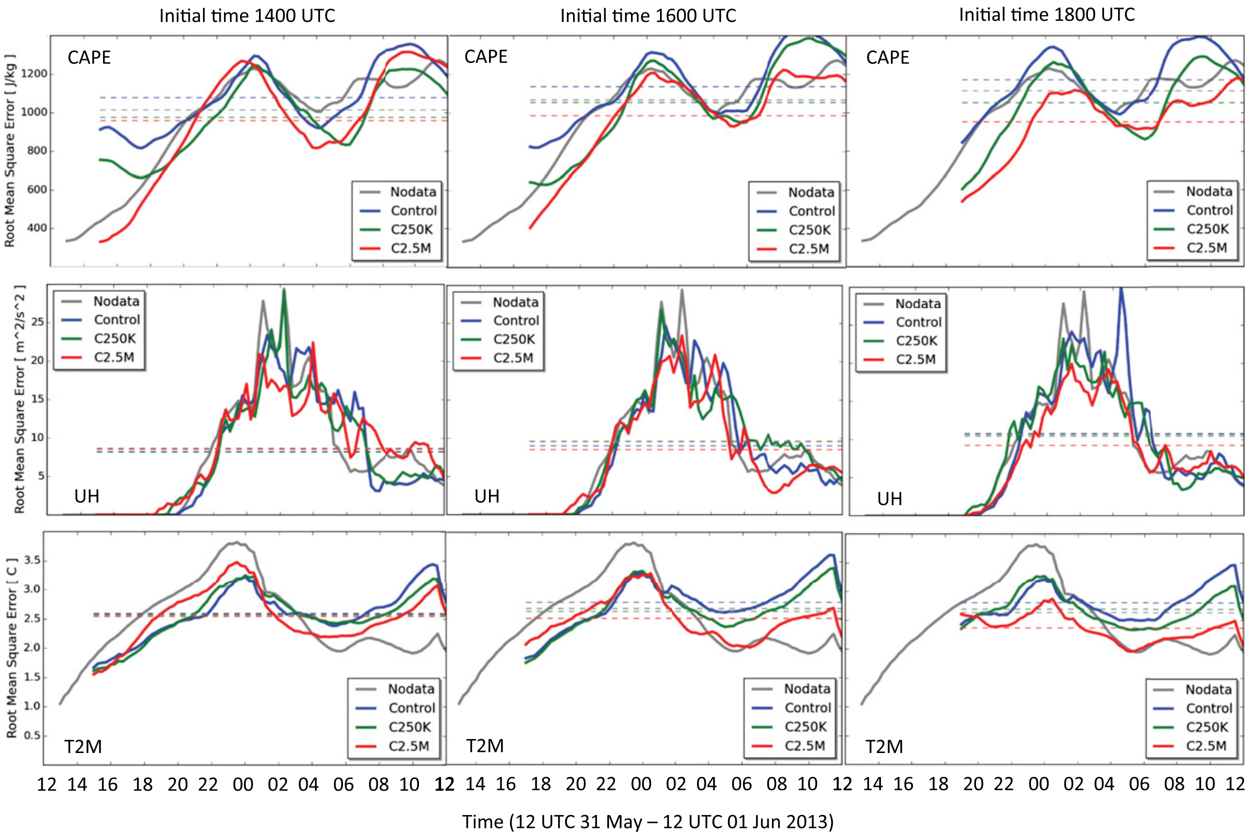

FIG. 6. RMS forecast error for (top) CAPE (J kg^{-1}), (middle) hourly maximum updraft helicity (UH) (m^2 s^{-2}), and (bottom) 2-m temperature (T2M, °C) for forecasts initialized from analyses at (left) 1400, (middle) 1600, and (right) 1800 UTC 31 May 2013. In each panel the RMS errors are shown for the Control experiment (blue), the ROSC-250K experiment (green, labeled "C250K"), the ROSC-2.5M experiment (red, labeled "C2.5M"), and the free-running forecast (gray, labeled "Nodata", repeated from left to right panels). Dashed lines using the same colors are plotted for the mean RMS error over the forecast period.

quickly becomes very difficult to detect due the noise caused by model errors.

6. Summary and conclusions

Experiments evaluating the impact of ROSCs in a severe weather QuickOSSE suggest the potential for high-resolution GNSS RO observations to refine the position and intensity and to reduce the analysis uncertainty of a dryline in the lower-tropospheric humidity field, as well as of features in the lower-tropospheric temperature field. This first mesoscale, severe weather application/evaluation of RO data showed very positive results for tropospheric moisture analysis and generally positive forecast impacts, albeit in the context of a single case study. In addition, our results suggest that ROSCs may also improve the forecast distribution of key environmental precursor controls for convection initiation and intensity (e.g., CAPE; capping inversions; midlevel dry layers; wind shear) by better analyzing the temperature and humidity variables; and improve the forecast timing and location of convective outbreaks.

In conclusion, our results suggest that observations from future hypothetical large ROSCs have significant potential to produce more accurate analyses in severe weather environments, and therefore, better characterize the environment for severe weather convective initiation. More accurate 3D analyses of temperature and water vapor in the lower troposphere are critical to improved severe weather forecasts. The forecast results are encouraging but limited by sample size and the ability of current models to forecast severe weather.

A number of caveats apply to this study. First, the impact of RO observations on severe weather analysis and forecasting should be examined for other diverse cases. Second, the nominal set of observations (i.e., those used in Control described in section 4c) does not include radar data. The lack of radar data is justified in this study because convection is minimal during the assimilation period, but other cases should be chosen to study the impact of combining RO and radar data. The approach of this study is helpful to demonstrate that the RO has useful information, but does not demonstrate that this information will still add value when other available observations are thoroughly exploited. Third, the additional, potentially valuable, impact of RO observations on correcting biases of other data types is not included in the current study. Fourth, several aspects of the OSSE system used here could be improved. All aspects of an OSSE system should be tuned and validated with respect to realism (Hoffman and Atlas 2016). While the NR described in section 2a is realistic in several aspects, only limited validation versus reality was performed. Choices of parameterization for the NR were made subjectively so that differences between the NR and reality were as small as possible. A subjective comparison of simulated and observed reflectivity images indicated that differences among the longer nonensemble forecasts (initialized at 1400, 1600, and 1800 UTC) and the NR were generally larger than differences between the NR and observed. A more thorough study of the forecast differences would be desirable, but should include additional cases. Some shortcuts to simulating the RO observations were taken, including the generation of tangent points, the use of the same forward model in simulating and assimilating observations, and the vertical thinning procedure. The WRF-DART system used, while advanced in using the EnKF approach is simplistic in some regards compared to an operational system. In particular the effect of variational bias correction (mentioned above) and quality control are not present in the experiments reported here.

Clearly there is more to do—this is a preliminary study and the quantitative results of simulation studies are not directly applicable to reality without thorough calibration and validation. However, in spite of the above caveats, the results of the current study do suggest the potential for RO observations to improve our ability to warn on forecast for severe weather events.

Acknowledgments. The authors thank Robert Atlas, Richard Anthes, Jon Kirchner, and Lidia Cucurull for helpful discussions relevant to this work. The authors thank the journal reviewers and Thomas Jones for their thorough and careful reviews and helpful suggestions and comments.

APPENDIX

Acronyms and Expansions

All acronyms used in the text are defined below. Acronyms used as units (e.g., UTC) and proper names (e.g., names of specific institutions and systems) are not expanded in the text.

Acronym	*Definition*
4D-Var	Four-dimensional variational data assimilation
ACM2	Asymmetrical Convective Model, version 2
AGL	Above ground level
AMV	Atmospheric motion vector
CAPE	Convective available potential energy
COSMIC	Constellation Observing System for Meteorology, Ionosphere and Climate
DA	Data assimilation
DART	Data Assimilation Research Testbed
dB*Z*	decibels of *Z* (reflectivity)
ECMWF	European Centre for Medium-Range Weather Forecasts
EF	Enhanced Fujita scale
EnKF	Ensemble Kalman filter
GNSS	Global Navigation Satellite System
GPS	Global positioning system
LEO	Low Earth orbit
MET	Model Evaluation Tools
MYJ	Mellor–Yamada–Janjić
MYNN	Mellor–Yamada–Nakanishi–Niino
NAM	North American Mesoscale Forecast System
NCAR	National Center for Atmospheric Research
NCEP	National Centers for Environmental Prediction
NME	NSSL Mesoscale Ensemble
NOAA	National Oceanic and Atmospheric Administration
Noah	NOAA/NCEP–Oregon State University–Air Force Research Laboratory–NOAA/Office of Hydrology land surface model
NR	Nature run
NSSL	National Severe Storms Laboratory (NOAA)
OSE	Observing system experiment
OSSE	Observing system simulation experiment
PBL	Planetary boundary layer
QC	Quality control
QuickOSSE	Quick OSSE
RMS	Root-mean-square
RO	Radio occultation
ROSC	RO superconstellations
RRTMG	Rapid Radiative Transfer Model for GCMs
T2M	2-m temperature
TP	Tangent point
UH	Maximum updraft helicity
UTC	Universal Time Coordinated
WRF	Weather Research and Forecasting Model
YSU	Yonsei University

REFERENCES

Anderson, J., T. Hoar, K. Raeder, H. Liu, N. Collins, R. Torn, and A. Avellano, 2009: The Data Assimilation Research Testbed: A community facility. *Bull. Amer. Meteor. Soc.*, **90**, 1283–1296, doi:10.1175/2009BAMS2618.1.

Atlas, R., and T. S. Pagano, 2014: Observing system simulation experiments to assess the potential impact of proposed satellite instruments on hurricane prediction. *Imaging Spectrometry XIX*, P. Mouroulis and T. S. Pagano, Eds., International Society for Optical Engineering (SPIE Proceedings, Vol. 9222), doi:10.1117/12.2063648.

——, L. Bucci, B. Annane, R. Hoffman, and S. Murillo, 2015: Observing system simulation experiments to assess the potential impact of new observing systems on hurricane forecasting. *Mar. Technol. Soc. J.*, **49**, 140–148, doi:10.4031/MTSJ.49.6.3.

Bingham, G., and Coauthors, 2013: Rapidly updated hyperspectral sounding and imaging data for severe storm prediction. *Infrared Remote Sensing and Instrumentation XXI*, M. Strojnik Scholl and Gonzalo Páez, Eds., International Society for Optical Engineering (SPIE Proceedings, Vol. 8867), doi:10.1117/12.2030687.

Bluestein, H. B., J. C. Snyder, and J. B. Houser, 2015: A multiscale overview of the El Reno, Oklahoma, tornadic supercell of 31 May 2013. *Wea. Forecasting*, **30**, 525–552, doi:10.1175/WAF-D-14-00152.1.

Chen, S. Y., C. Y. Huang, Y. H. Kuo, Y. R. Guo, and S. Sokolovskiy, 2009: Assimilation of GPS refractivity from FORMOSAT-3/COSMIC using a nonlocal operator with WRF 3DVAR and its impact on the prediction of a typhoon event. *Terr. Atmos. Oceanic Sci.*, **20**, 133–154, doi:10.3319/TAO.2007.11.29.01(F3C).

Chen, Y.-C., M.-E. Hsieh, L.-F. Hsiao, Y.-H. Kuo, M.-J. Yang, C.-Y. Huang, and C.-S. Lee, 2015: Systematic evaluation of the impacts of GPSRO data on the prediction of typhoons over the northwestern Pacific in 2008–2010. *Atmos. Meas. Tech.*, **8**, 2531–2542, doi:10.5194/amt-8-2531-2015.

Chou, M.-D., and M. J. Suarez, 1999: A solar radiation parameterization (CLIRAD-SW) for atmospheric studies (Tech. Memo. 1999-104606). *A Solar Radiation Parameterization for Atmospheric Studies*, M.-D. Chou and M. J. Suarez, Eds., Technical Report Series on Global Modeling and Data Assimilation, Vol. 15, NASA, Goddard Space Flight Center, Greenbelt, MD, 38 pp. [Available online at http://www2.mmm.ucar.edu/wrf/users/phys_refs/SW_LW/Goddard_part1.pdf.]

——, ——, X.-Z. Liang, and M. M.-H. Yan, 2001: A thermal infrared radiation parameterization for atmospheric studies (Tech. Memo. 2001-104606). *A Thermal Infrared Radiation Parameterization for Atmospheric Studies*, M. J. Suarez, Ed., Technical Report Series on Global Modeling and Data Assimilation, Vol. 19, NASA, Goddard Space Flight Center, Greenbelt, MD, 55 pp. [Available online at http://www2.mmm.ucar.edu/wrf/users/phys_refs/SW_LW/Goddard_part2.pdf.]

Clark, A. J., J. Gao, P. T. Marsh, T. Smith, J. S. Kain, J. Correia, Jr., M. Xue, and F. Kong, 2013: Tornado pathlength forecasts from 2010 to 2011 using ensemble updraft helicity. *Wea. Forecasting*, **28**, 387–407, doi:10.1175/WAF-D-12-00038.1.

COESA, 1976: *U.S. Standard Atmosphere, 1976*. NOAA, 227 pp.

Cucurull, L., and J. C. Derber, 2008: Operational implementation of COSMIC observations into NCEP's global data assimilation system. *Wea. Forecasting*, **23**, 702–711, doi:10.1175/2008WAF2007070.1.

——, ——, R. Treadon, and R. J. Purser, 2007: Assimilation of Global Positioning System radio occultation observations into NCEP's global data assimilation system. *Mon. Wea. Rev.*, **135**, 3174–3193, doi:10.1175/MWR3461.1.

Data Assimilation Research Testbed, 2016: DART Lanai Release Notes. NCAR, Boulder, CO, accessed 7 April 2014. [Available online at http://www.image.ucar.edu/DAReS/DART/Lanai_release.html.]

Ek, M. B., K. E. Mitchell, Y. Lin, E. Rogers, P. Grunmann, V. Koren, G. Gayno, and J. D. Tarpley, 2003: Implementation of Noah land-surface model advances in the NCEP operational mesoscale Eta model. *J. Geophys. Res.*, **108**, 8851, doi:10.1029/2002JD003296.

Fujita, T., D. J. Stensrud, and D. C. Dowell, 2007: Surface data assimilation using an ensemble Kalman filter approach with initial condition and model physics uncertainties. *Mon. Wea. Rev.*, **135**, 1846–1868, doi:10.1175/MWR3391.1.

Gilliam, R. C., and J. E. Pleim, 2010: Performance assessment of new land surface and planetary boundary layer physics in the WRF-ARW. *J. Appl. Meteor. Climatol.*, **49**, 760–774, doi:10.1175/2009JAMC2126.1.

Grell, G. A., and S. R. Freitas, 2014: A scale and aerosol aware stochastic convective parameterization for weather and air quality modeling. *Atmos. Chem. Phys.*, **14**, 5233–5250, doi:10.5194/acp-14-5233-2014.

Greybush, S. J., E. Kalnay, T. Miyoshi, K. Ide, and B. R. Hunt, 2011: Balance and ensemble Kalman filter localization techniques. *Mon. Wea. Rev.*, **139**, 511–522, doi:10.1175/2010MWR3328.1.

Hajj, G. A., E. R. Kursinski, L. J. Romans, W. I. Bertiger, and S. S. Leroy, 2002: A technical description of atmospheric sounding by GPS occultation. *J. Atmos. Sol.-Terr. Phys.*, **64**, 451–469, doi:10.1016/S1364-6826(01)00114-6.

Healy, S. B., 2008: Forecast impact experiment with a constellation of GPS radio occultation receivers. *Atmos. Sci. Lett.*, **9**, 111–118, doi:10.1002/asl.169.

Hoffman, R. N., and R. Atlas, 2016: Future observing system simulation experiments. *Bull. Amer. Meteor. Soc.*, **97**, 1601–1616, doi:10.1175/BAMS-D-15-00200.1.

Hong, S.-Y., Y. Noh, and J. Dudhia, 2006: A new vertical diffusion package with an explicit treatment of entrainment processes. *Mon. Wea. Rev.*, **134**, 2318–2341, doi:10.1175/MWR3199.1.

Iacono, M. J., J. S. Delamere, E. J. Mlawer, M. W. Shephard, S. A. Clough, and W. D. Collins, 2008: Radiative forcing by long-lived greenhouse gases: Calculations with the AER radiative transfer models. *J. Geophys. Res.*, **113**, D13103, doi:10.1029/2008JD009944.

Janjić, Z., 1994: The step-mountain Eta coordinate model: Further developments of the convection, viscous sublayer, and turbulence closure schemes. *Mon. Wea. Rev.*, **122**, 927–945, doi:10.1175/1520-0493(1994)122<0927:TSMECM>2.0.CO;2.

——, 2002: Nonsingular implementation of the Mellor-Yamada level 2.5 scheme in the NCEP Meso model. Office Note 437, NCEP, Washington, DC, 61 pp.

Jirak, I. L., and Coauthors, 2014: An overview of the 2013 NOAA Hazardous Weather Testbed Spring Forecasting Experiment. *26th Conf. on Weather Analysis and Forecasting/22nd Conf. on Numerical Weather Prediction*, Atlanta, GA, Amer. Meteor. Soc., J11.1. [Available online at https://ams.confex.com/ams/94Annual/webprogram/Paper239754.html.]

Jones, T. A., J. A. Otkin, D. J. Stensrud, and K. Knopfmeier, 2013: Assimilation of satellite infrared radiances and Doppler radar observations during a cool season observing system simulation experiment. *Mon. Wea. Rev.*, **141**, 3273–3299, doi:10.1175/MWR-D-12-00267.1.

——, D. Stensrud, L. Wicker, P. Minnis, and R. Palikonda, 2015: Simultaneous radar and satellite data storm-scale assimilation using an ensemble Kalman filter approach for 24 May 2011. *Mon. Wea. Rev.*, **143**, 165–194, doi:10.1175/MWR-D-14-00180.1.

——, K. Knopfmeier, D. Wheatley, G. Creager, P. Minnis, and R. Palikonda, 2016: Storm-scale data assimilation and ensemble forecasting with the NSSL experimental warn-on-forecast system. Part II: Combined radar and satellite data experiments. *Wea. Forecasting*, **31**, 297–327, doi:10.1175/WAF-D-15-0107.1.

Kain, J. S., 2004: The Kain–Fritsch convective parameterization: An update. *J. Appl. Meteor.*, **43**, 170–181, doi:10.1175/1520-0450(2004)043<0170:TKCPAU>2.0.CO;2.

——, and J. M. Fritsch, 1993: Convective parameterization for mesoscale models: The Kain–Fritsch scheme. *The Representation of Cumulus Convection in Numerical Models*, *Meteor. Monogr.*, No. 24, Amer. Meteor. Soc., 165–170.

Kalnay, E., 2002: *Atmospheric Modeling, Data Assimilation, and Predictability.* Cambridge University Press, 364 pp.

Kerr, C. A., D. J. Stensrud, and X. Wang, 2015: Assimilation of cloud-top temperature and radar observations of an idealized splitting supercell using an observing system simulation experiment. *Mon. Wea. Rev.*, **143**, 1018–1034, doi:10.1175/MWR-D-14-00146.1.

Kunii, M., H. Seko, M. Ueno, Y. Shoji, and T. Tsuda, 2012: Impact of assimilation of GPS radio occultation refractivity on the forecast of Typhoon Usagi in 2007. *J. Meteor. Soc. Japan*, **90**, 255–273, doi:10.2151/jmsj.2012-207.

Kursinski, E. R., and G. A. Hajj, 2001: A comparison of water vapor derived from GPS occultations and global weather analyses. *J. Geophys. Res.*, **106**, 1113–1138, doi:10.1029/2000JD900421.

——, ——, J. T. Schofield, R. P. Linfield, and K. R. Hardy, 1997: Observing Earth's atmosphere with radio occultation measurements using the Global Positioning System. *J. Geophys. Res.*, **102**, 23 429–23 465, doi:10.1029/97JD01569.

Lambrigtsen, B. H., 2015: Progress in developing a geostationary microwave sounder. *11th Annual Symp. on New Generation Operational Environmental Satellite Systems*, Phoenix, AZ, Amer. Meteor. Soc., J19.3. [Available online at https://ams.confex.com/ams/95Annual/webprogram/Paper267078.html.]

Li, X., F. Zus, C. Lu, T. Ning, G. Dick, M. Ge, J. Wickert, and H. Schuh, 2015: Retrieving high-resolution tropospheric gradients from multiconstellation GNSS observations. *Geophys. Res. Lett.*, **42**, 4173–4181, doi:10.1002/2015GL063856.

Liu, H., J. Anderson, Y.-H. Kuo, C. Snyder, and A. Caya, 2008: Evaluation of a nonlocal quasi-phase observation operator in assimilation of CHAMP radio occultation refractivity with WRF. *Mon. Wea. Rev.*, **136**, 242–256, doi:10.1175/2007MWR2042.1.

Ma, Z., Y.-H. Kuo, F. M. Ralph, P. J. Neiman, G. A. Wick, E. Sukovich, and B. Wang, 2011: Assimilation of GPS radio occultation data for an intense atmospheric river with the NCEP regional GSI system. *Mon. Wea. Rev.*, **139**, 2170–2183, doi:10.1175/2011MWR3342.1.

Maschhoff, K., 2015: MISTiC winds, a distributed architecture approach to dynamic weather observations. *Fifth Conf. on Transition of Research to Operations*, Phoenix, AZ, Amer. Meteor. Soc., 2.2. [Available online at https://ams.confex.com/ams/95Annual/webprogram/Paper269044.html.]

Melbourne, W. G., and Coauthors, 1994: The application of spaceborne GPS to atmospheric limb sounding and global change monitoring. JPL Publ. 94-18, NASA Jet Propulsion Laboratory, Pasadena, CA, 147 pp. [Available online at https://ntrs.nasa.gov/archive/nasa/casi.ntrs.nasa.gov/19960008694.pdf.]

Nakanishi, M., and H. Niino, 2006: An improved Mellor–Yamada Level-3 model: Its numerical stability and application to a regional prediction of advection fog. *Bound.-Layer Meteor.*, **119**, 397–407, doi:10.1007/s10546-005-9030-8.

——, and ——, 2009: Development of an improved turbulence closure model for the atmospheric boundary layer. *J. Meteor. Soc. Japan*, **87**, 895–912, doi:10.2151/jmsj.87.895.

Pan, Y., K. Zhu, M. Xue, X. Wang, M. Hu, S. G. Benjamin, S. S. Weygandt, and J. S. Whitaker, 2014: A GSI-based coupled EnSRF-En3DVar hybrid data assimilation system for the operational rapid refresh model: Tests at a reduced resolution. *Mon. Wea. Rev.*, **142**, 3756–3780, doi:10.1175/MWR-D-13-00242.1.

Pleim, J. E., 2007a: A combined local and nonlocal closure model for the atmospheric boundary layer. Part I: Model description and testing. *J. Appl. Meteor. Climatol.*, **46**, 1383–1395, doi:10.1175/JAM2539.1.

——, 2007b: A combined local and nonlocal closure model for the atmospheric boundary layer. Part II: Application and evaluation in a mesoscale meteorological model. *J. Appl. Meteor. Climatol.*, **46**, 1396–1409, doi:10.1175/JAM2534.1.

——, and A. Xiu, 2003: Development of a land surface model. Part II: Data assimilation. *J. Appl. Meteor.*, **42**, 1811–1822, doi:10.1175/1520-0450(2003)042<1811:DOALSM>2.0.CO;2.

Poli, P., 2004: Effects of horizontal gradients on GPS radio occultation observation operators. II: A fast atmospheric refractivity gradient operator (FARGO). *Quart. J. Roy. Meteor. Soc.*, **130**, 2807–2825, doi:10.1256/qj.03.229.

Schwartz, C. S., G. S. Romine, R. A. Sobash, K. R. Fossell, and M. L. Weisman, 2015a: NCAR's experimental real-time convection-allowing ensemble prediction system. *Wea. Forecasting*, **30**, 1645–1654, doi:10.1175/WAF-D-15-0103.1.

——, ——, M. L. Weisman, R. A. Sobash, K. R. Fossell, K. W. Manning, and S. B. Trier, 2015b: A real-time convection-allowing ensemble prediction system initialized by mesoscale ensemble Kalman filter analyses. *Wea. Forecasting*, **30**, 1158–1181, doi:10.1175/WAF-D-15-0013.1.

Skamarock, W. C., and J. B. Klemp, 2008: A time-split nonhydrostatic atmospheric model for weather research and forecasting applications. *J. Comput. Phys.*, **227**, 3465–3485, doi:10.1016/j.jcp.2007.01.037.

——, and Coauthors, 2008: A description of the Advanced Research WRF version 3. NCAR Tech. Note NCAR/TN-475+STR, 113 pp., doi:10.5065/D68S4MVH.

Snook, N., M. Xue, and Y. Jung, 2015: Multiscale EnKF assimilation of radar and conventional observations and ensemble forecasting for a tornadic mesoscale convective system. *Mon. Wea. Rev.*, **143**, 1035–1057, doi:10.1175/MWR-D-13-00262.1.

Sokolovskiy, S., Y.-H. Kuo, and W. Wang, 2005: Assessing the accuracy of a linearized observation operator for assimilation of radio occultation data: Case simulations with a high-resolution weather model. *Mon. Wea. Rev.*, **133**, 2200–2212, doi:10.1175/MWR2948.1.

Stensrud, D. J., J.-W. Bao, and T. T. Warner, 2000: Using initial condition and model physics perturbations in short-range ensemble simulations of mesoscale convective systems. *Mon. Wea. Rev.*, **128**, 2077–2107, doi:10.1175/1520-0493(2000)128<2077:UICAMP>2.0.CO;2

——, and Coauthors, 2009: Convective-scale warn-on-forecast system: A vision for 2020. *Bull. Amer. Meteor. Soc.*, **90**, 1487–1499, doi:10.1175/2009BAMS2795.1.

Tewari, M., and Coauthors, 2004: Implementation and verification of the unified Noah land surface model in the WRF model. *20th Conf. on Weather Analysis and Forecasting/16th Conf. on Numerical Weather Prediction*, Seattle, WA, Amer. Meteor. Soc., 14.2a. [Available online at https://ams.confex.com/ams/84Annual/techprogram/paper_69061.htm.]

Thompson, G., R. M. Rasmussen, and K. Manning, 2004: Explicit forecasts of winter precipitation using an improved bulk microphysics scheme. Part I: Description and sensitivity analysis. *Mon. Wea. Rev.*, **132**, 519–542, doi:10.1175/1520-0493(2004)132<0519:EFOWPU>2.0.CO;2.

——, P. R. Field, R. M. Rasmussen, and W. D. Hall, 2008: Explicit forecasts of winter precipitation using an improved bulk microphysics scheme. Part II: Implementation of a new snow parameterization. *Mon. Wea. Rev.*, **136**, 5095–5115, doi:10.1175/2008MWR2387.1.

Tiedtke, M., 1989: A comprehensive mass flux scheme for cumulus parameterization in large-scale models. *Mon. Wea. Rev.*, **117**, 1779–1800, doi:10.1175/1520-0493(1989)117<1779:ACMFSF>2.0.CO;2.

Ware, R., and Coauthors, 1996: GPS sounding of the atmosphere from low earth orbit: Preliminary results. *Bull. Amer. Meteor. Soc.*, **77**, 19–40, doi:10.1175/1520-0477(1996)077<0019:GSOTAF>2.0.CO;2.

Weisman, M. L., and Coauthors, 2015: The Mesoscale Predictability Experiment (MPEX). *Bull. Amer. Meteor. Soc.*, **96**, 2127–2149, doi:10.1175/BAMS-D-13-00281.1.

Wheatley, D. M., K. H. Knopfmeier, T. A. Jones, and G. J. Creager, 2015: Storm-scale data assimilation and ensemble forecasting with the NSSL experimental warn-on-forecast system. Part I: Radar data experiments. *Wea. Forecasting*, **30**, 1795–1817, doi:10.1175/WAF-D-15-0043.1.

Wurman, J., K. Kosiba, P. Robinson, and T. Marshall, 2014: The role of multiple-vortex tornado structure in causing storm researcher fatalities. *Bull. Amer. Meteor. Soc.*, **95**, 31–45, doi:10.1175/BAMS-D-13-00221.1.

Xiu, A., and J. E. Pleim, 2001: Development of a land surface model. Part I: Application in a mesoscale meteorological model. *J. Appl. Meteor.*, **40**, 192–209, doi:10.1175/1520-0450(2001)040<0192:DOALSM>2.0.CO;2.

Yussouf, N., J. Gao, D. J. Stensrud, and G. Ge, 2013a: The impact of mesoscale environmental uncertainty on the prediction of a tornadic supercell storm using ensemble data assimilation approach. *Adv. Meteor.*, **2013**, 731647, doi:10.1155/2013/731647.

——, E. R. Mansell, L. J. Wicker, D. M. Wheatley, and D. J. Stensrud, 2013b: The ensemble Kalman filter analyses and forecasts of the 8 May 2003 Oklahoma City tornadic supercell storm using single- and double-moment microphysics schemes. *Mon. Wea. Rev.*, **141**, 3388–3412, doi:10.1175/MWR-D-12-00237.1.

Zhang, C., Y. Wang, and K. Hamilton, 2011: Improved representation of boundary layer clouds over the southeast Pacific in ARW-WRF using a modified Tiedtke cumulus parameterization scheme. *Mon. Wea. Rev.*, **139**, 3489–3513, doi:10.1175/MWR-D-10-05091.1.

Zou, X., Y.-H. Kuo, and Y.-R. Guo, 1995: Assimilation of atmospheric radio refractivity using a nonhydrostatic adjoint model. *Mon. Wea. Rev.*, **123**, 2229–2250, doi:10.1175/1520-0493(1995)123<2229:AOARRU>2.0.CO;2.